

# Bright LaF<sub>3</sub>:Eu@Ir Phosphors Combining Two-Photon Excitation, $d \rightarrow f$ Energy Transfer and Tunable Time-Gated Chromaticity for Multicolor Cell Imaging

Yating Ye, Mattia Bramini, Paola Sánchez-Moreno,\* Angel Orte,\* Juan-Ramón Jiménez, and Juan Manuel Herrera\*

In order to advance the practical applications of photoluminescence lanthanide-based nanoparticles (LnNPs), it is essential to minimize quenching by surface defects and to enhance the efficiency of lanthanide excitation. Surface functionalization with organic antennas has proven effective in preparing dye-sensitized LnNPs with enhanced photoluminescence performance. Nevertheless, the limited chemical and photochemical stability of the organic dyes hinders the practical applications of these composites. This report presents Eu-doped LaF<sub>3</sub> submicron particles (EuLa<sub>SMDs</sub>) and analogue small nanoparticles (EuLa<sub>NPs</sub>) functionalized with a robust Ir<sup>III</sup> complex (Ir1) as antenna. The EuLa<sub>SMDs</sub>@Irl and EuLa<sub>NPs</sub>@Irl hybrids exhibit a combination of short-lived Ir-based (yellow) and long-lived Eu-based (red) emissions, which can be selectively detected by time-gated detection. Following Ir1-sensitization, the Eu-based emission is amplified, reaching up to 307-fold (for EuLa<sub>SMDs</sub>@Ir1) and 188-fold (for EuLa<sub>NPs</sub>@Ir1), compared to that exhibited by pristine phosphors. Efficient Ir1-sensitized Eu<sup>III</sup>-based emission can also be achieved using NIR excitation, as Ir1 exhibits a moderate cross-section of  $\sigma_2 = 4.6 \pm 0.6$  GM at  $\lambda = 800$  nm. Both hybrids demonstrate effective internalization in HEK-293 cells with no observed toxicity at concentrations relevant to biomedical applications. Cells are imaged by TG-imaging and PLIM microscopy. Following UV-vis ( $\lambda_{\rm exc} = 375$  nm) or NIR ( $\lambda_{\rm exc} = 800$  nm) excitation, overlapped Ir1- and Eu-based emissions are detected.

1. Introduction

Fluoride-based nanoparticles doped with optically active lanthanide ions (LnNPs) exhibit remarkable luminescence

properties of interest in fields as diverse as lighting, anti-counterfeiting, bioimaging and phototherapy.[1-6] These materials exhibit excellent photostability, tunable colour emission as a function of the selected luminescent lanthanide ions, and very long-lived excited states due to the low phonon energy of the fluoride matrix, which minimizes non-radiative relaxation pathways.[7,8] However, due to their intrinsically high surfaceto-volume ratio, and also due to the fact that the emissive dopant ions tend to be preferentially located at the outermost surface of the nanoparticles as their size decreases, a high fraction of the emissive centers interact with surfactants, solvent molecules, or other impurities present in the medium. As a results, these emissive centers suffer severe surface quenching effects.[9,10] Moreover, the extremely narrow and low absorption of the forbidden f-f transitions necessitates the use of high-intensity excitation sources at a limited set of specific excitation wavelengths to effectively sensitize Ln<sup>III</sup> emission. These factors limit the luminescence intensity of LnNPs and, consequently, their potential applications.[11–13]

An effective strategy for enhancing the emission brightness of LnNPs has been the use of organic chromophores as capping ligands to functionalize the surface of these LnNPs.<sup>[14,15]</sup> The use of organic dyes provides protection for photoactive metal

Y. Ye, J.-R. Jiménez, J. M. Herrera

Departamento de Química Inorgánica y Unidad de Excelencia de Química Aplicada a Biomedicina y Medioambiente. Universidad de Granada

Facultad de Ciencias

Campus Fuentenueva, Granada 18071, Spain

E-mail: jmherrera@ugr.es

M. Bramini

Departamento de Biología Celular Universidad de Granada Facultad de Ciencias

Campus Fuentenueva, Granada 18071, Spain

The ORCID identification number(s) for the author(s) of this article can be found under https://doi.org/10.1002/adom.202500717

DOI: 10.1002/adom.202500717

P. Sánchez-Moreno Departamento de Física Aplicada Universidad de Granada Campus Fuentenueva, Granada 18071, Spain E-mail: paolasm@ugr.es

A. Orte

Nanoscopy-UGR Laboratory. Departamento de Fisicoquímica y Unidad de Excelencia de Química Aplicada a Biomedicina y Medioambiente. Universidad de Granada

Universidad de Granada Facultad de Farmacia

Campus Cartuja, Granada 18071, Spain

E-mail: angelort@ugr.es

ADVANCED
OPTICAL
MATERIALS

21951071, 0, Downloaded from https://adarced.onlinelbitary.wiley.com/doi/10.1002/ador.20250717 by Cochametalia, Wiley Online Library on [2906/2025]. See the Terms and Conditions (https://onlinelbitary.wiley.com/terms-and-conditions) on Wiley Online Library for rules of use; OA articles are governed by the applicable Creative Commons Licenses

ions on the surface of LnNPs from solvent and/or surfactant interactions and quenching. Additionally, the high absorption cross-section of these dyes makes them optimal light-harvesting units, enabling sensitized lanthanide emission through dye  $\rightarrow$  lanthanide energy transfer (EnT), which is known as the Antenna effect. Consequently, recent successes in hybrid dye-lanthanide nanocomposite systems (LnNPs@dye), including dye-sensitized downshifting, dye-sensitized downconversion, dye-sensitized upconversion (UC), and UCNPs-dye energy transfer nanoparticles, have been achieved. These developments have created new possibilities for a diverse range of biomedical and photonics applications.  $^{[16,17]}$ 

Recently, our research group<sup>[18]</sup> and others<sup>[19]</sup> have demonstrated that the use of coordination metal complexes as antenna groups can result in the development of a new generation of d-f LnNPs hybrids with enhanced photophysical properties. Compared to organic dyes, d-block chromophores display superior chemical and photochemical stability and can be functionalized with carboxylate or phosphonate groups to facilitate efficient anchoring to the LnNPs surface. Among d-block chromophores, IrIII complexes have been effectively used as lightharvesting units to sensitize lanthanide emission.<sup>[20]</sup> Specifically, we reported the synthesis of Eu-doped LaF<sub>3</sub> particles functionalized with a blue-emissive  $Ir^{III}$  complex, where effective  $Ir \rightarrow Eu$ EnT was demonstrated.[18] The LaF<sub>3</sub>:Eu@Ir composite exhibited amplified EuIII-based emission combined with bright IrIII-based emission and color tunable luminescence, which depended on which of the  $Ir^{\rm III}$  or  $Eu^{\rm III}$  centers were excited preferentially. Furthermore, the IrIII complex exhibited a moderate two-photon absorption (TPA) cross-section, enabling the observation of sensitized EuIII emission following near-infrared excitation of the IrIII moieties. These results indicated that a new generation of brighter and chromatic LnNPs composites could be prepared using d-block chromophores as antennas. This approach offers an alternative to the organic dyes considered thus far.

In order to confirm the ability of IrIII complexes to sensitize Eu<sup>III</sup> -based emission in LaF<sub>3</sub>:Eu phosphors and with the aim of improving the emissive performance of these hybrid df composites, we present here our results using the Ir<sup>III</sup> complex [Ir(dfppy)<sub>2</sub>(H<sub>2</sub>dcbpy)](PF<sub>6</sub>) (Ir1) as, in principle, an ideal sensitizer moiety. In this complex, the metal center is coordinated to two 2-(2,4-difluorophenyl)pyridinate ligands (dfppy) and a 2,2'bipyridine moiety bearing two carboxylic groups (H2dcbpy: 2,2'bypiridine-4,4'-dicarboxylic acid). This complex displays a yellow emission that primarily originates from a 3MLCT excited state, which is predominantly localized within the H<sub>2</sub>dcbpy ligand.<sup>[21]</sup> The carboxylic groups of this ligand can act as efficient anchoring groups, coordinating the surface of LaF<sub>3</sub>:Eu particles. Consequently, the distance between the donor (Ir) and acceptor (Eu) centers will be minimized, thereby enhancing the probability of  $Ir \rightarrow Eu EnT$ .

Furthermore, in order to determine the impact of particle size on the luminescence performance of the LaF<sub>3</sub>:Eu@Ir hybrids, two types of composites were prepared: submicron LaF<sub>3</sub>:Eu disks (EuLa<sub>SMDs</sub>) and much smaller LaF<sub>3</sub>:Eu NPs (EuLa<sub>NPs</sub>). As the particle size decreases, the concentration of photoactive Eu<sup>III</sup> ions on the surface (Eu<sub>surface</sub>) increases, thereby favoring quenching by surface defects. [9,10,22] This ultimately results in a decrease in the overall Eu<sup>III</sup> emission for pristine LaF<sub>3</sub>:Eu samples. In con-

trast, for LaF<sub>3</sub>:Eu@Ir hybrids, a higher fraction of Eu<sub>surface</sub> centers implies a greater likelihood of forming coordinated Ir – Eu<sub>surface</sub> pairs, where nonradiative Ir  $\rightarrow$  Eu EnT, a short range process, can occur efficiently leading, in theory, to enhanced Eu<sup>III</sup> emission.

One of the major advantages of long-lived phosphors, especially lanthanide-based probes, is their suitability as PL imaging agents for biological applications. Their long lifetimes exceed those of potential fluorescent interferants in biological and other complex media. This makes them particularly useful in timegated (TG) imaging, a robust imaging technique that provides background-free imaging. TG imaging works by filtering photons according to their arrival time, effectively discarding signals from biological luminescent species, such as proteins, collagen and NADPH. As a result, this approach enhances both sensitivity and selectivity. [23]

Another specialized, related technique is PL lifetime imaging (PLIM), which provides an additional level of quantitative information by simultaneously quantifying the luminescence lifetime of the detected probes. Therefore, lanthanide-based agents are receiving increasing attention as probes for cellular imaging and other biomedically relevant applications. [24,25] To explore the potential use of **Eula<sub>SMDs</sub>@Ir1** and **Eula<sub>NPs</sub>@Ir1** as bioimaging agents, both composites were exposed to HEK-293 cells and their bionanointeractions and internalization were investigated through TG-imaging and PLIM microscopy.

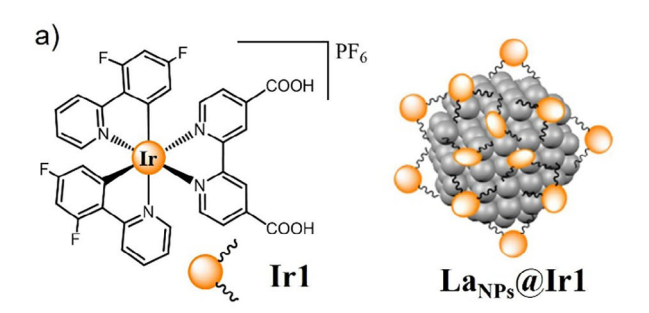
#### 2. Results and Discussion

#### 2.1. Photophysical Properties of Ir1 and La<sub>NPs</sub>@Ir1

The Ir<sup>III</sup> complex [Ir(dfppy)<sub>2</sub>(H<sub>2</sub>dcbpy)]PF<sub>6</sub> (Ir1) (Figure 1a) was prepared according to the procedure described by Jiang et al.[21] with some minor modifications (see SI, section 1). According to these authors, Ir1 exhibits an intense and non-structured emission band centered in the yellow spectroscopic region. This emission originates primarily from a <sup>3</sup>MLCT excited state with some mixing with  $^3LLCT$  (  $\pi_{dfppy} \to \pi^*_{~H2dcbpy}$  ) and  $^3LC$  (  $\pi_{dfppy} \to \pi^*_{~dfppy}$  ) excited states, which are very close in energy. The ability of Ir1 to be excited through a Two-Photon Absorption (TPA) process has been previously demonstrated.[26] However, its TPA crosssection  $(\sigma_2)$  was not reported. We calculated this parameter by irradiating a solution of Ir1 in dimethylformamide (DMF) with an ultrafast Titanium-Sapphire laser at  $\lambda_{\rm exc} = 800$  nm. The observed emission profile was very similar to that observed previously by single-photon excitation (Figure S1a, Supporting Information) and a TPA cross-section value of  $\sigma_2 = 4.6 \pm 0.6$  GM was determined using fluoresceine as standard.<sup>[27]</sup> Although this value is lower than that of other IrIII complexes with optimized TPA properties, [28-30] it is sufficient to achieve intense Ir-based emission under NIR laser excitation.

To determine the emissive properties of **Ir1** once it is coordinated to the surface of LnNPs, we first functionalized the surface of pure non-emissive LaF<sub>3</sub> nanoparticles (**La**<sub>NPs</sub>) with this complex. The resulting **La**<sub>NPs</sub>@**Ir1** hybrid dispersed in water exhibited intense excitation bands extending from the UV to the visible ( $\approx$ 450 nm) spectroscopic regions and an intense yellow emission centered at  $\lambda_{\rm em} = 556$  nm (Figure 1). The Ir-based emission decay could be fitted to a biexponential function with an average

Downloaded from https://advanced.onlinelibrary.wiley.com/doi/10.1002/adom.202500717 by Cochraneltalia, Wiley Online Library on [2906/2025]. See the Terms and Conditions (https://onlinelibrary.wiley.com/terms-and-conditions) on Wiley Online Library for rules of use; OA articles are governed by the applicable Creative Commons Licenses



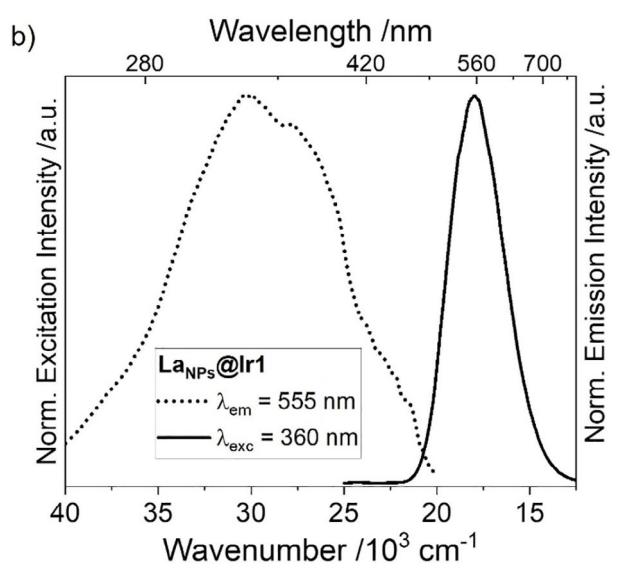


**Figure 1.** a) Schematic representation of complex **Ir1** (left) and composite **La**<sub>NPs</sub>@**Ir1** (right). b) Excitation (dotted line) and emission (full line) spectra of **La**<sub>NPs</sub>@**Ir1** dispersed in water (5 mg /3 mL).

lifetime of  $\tau_{\rm av} = 322 \pm 16$  ns (Figure S1b, Supporting Information).

# 2.2. Synthesis, Structural and Photophysical Properties of Bare Eu-Doped LaF<sub>3</sub> Particles (EuLa)

Two distinct types of EuIII-doped LaF3 particles, exhibiting notable differences in morphology and size, were synthesized via rapid and well-established microwave-assisted procedures previously described in detail.[31,32] In both cases, an Eu:La doping ratio of 30:70 was employed, as this ratio typically offers an optimal balance between the highest number of emitting Eu<sup>III</sup> centers and the least concentration quenching effects.[33] The use of the ionic liquid [BMIM]BF<sub>4</sub> (BMIM = 1-butyl-3-methylimidazolium) as a fluoride source resulted in the formation of  $Eu_{0.3}La_{0.7}F_3$  submicron disks (EuLa<sub>SMDs</sub>). As we reported previously, [18] these particles exhibit an average diameter and thickness close to 252 and 121 nm, respectively. The replacement of the [BMIM]BF<sub>4</sub> with NH<sub>4</sub>F as a fluoride source resulted in a significant change in the morphology and size of the obtained particles, which now formed pseudo-spherical  $Eu_{0.3}La_{0.7}F_3$  nanoparticles ( $EuLa_{NPs}$ ) with an average diameter of ≈35 nm (Figure S2, Supporting Information). Energy-dispersive X-ray spectroscopy experiments (Figure S2e, Supporting Information) corroborated the coexistence of  $La^{\rm III}$  and  $Eu^{\rm III}$  ions within the nanoparticles. Both  $EuLa_{\rm SMDs}$  and  $EuLa_{\rm NPs}$  particles are crystalline, and their diffraction patterns can be indexed with that of hexagonal  $LaF_3$  (tysonite phase, ICDD No. 01-082-0690) (Figure S3 and Table S1, Supporting Information).

The excitation and emission spectra of EuLa<sub>NPs</sub> and EuLa<sub>SMDs</sub> dispersed in water exhibited analogous patterns, as illustrated in Figures 2 and S4, Supporting Information, respectively. The excitation spectra, monitored at  $\lambda_{\rm em}$  = 591 nm, showed the characteristic Eu<sup>III</sup> excitation peaks, the most intense centered at  $\lambda$  = 396 nm (transition  ${}^5L_6 \leftarrow {}^7F_0$ ). Upon irradiation at  $\lambda_{\rm exc} = 396$  nm, the emission spectra showed the expected  ${}^5D_0 \rightarrow {}^7F_1$  (J = 1 – 4) emission bands with their maxima centered at 591 nm (I = 1), 616 nm (J = 2), 650 nm (J = 3) and 693 nm (J = 4). For both samples, the intensity of the  ${}^5D_0 \rightarrow {}^7F_1$  transition is higher than that of the  ${}^5D_0 \rightarrow {}^7F_2$  transition, providing evidence that the majority of the EuIII centers are located at centrosymmetric crystallographic sites, as expected for a LaF<sub>3</sub>-tysonite matrix where the metal ions occupy crystallographic sites with a C<sub>2</sub> symmetry.<sup>[34]</sup> The  ${}^5D_0 \rightarrow {}^7F_1$  transition is a magnetic dipole (MD) allowed transition, and its intensity, generally considered constant, is largely independent of the coordination sphere around the Eu<sup>III</sup> centers. The electric dipole (ED) allowed transitions  $^5D_0 \rightarrow {}^7F_{2.4}$ , are forbidden for centrosymmetric Eu<sup>III</sup> centers, although slight deviations of perfect inversion symmetry around the EuIII sites and the existence of crystal defects, such as surface defects, allow these transitions to gain intensity. This is particularly true for the so-called hypersensitive  ${}^5D_0 \rightarrow {}^7F_2$  transition, whose intensity is much more influenced by the local symmetry of the Eu<sup>III</sup> ions and the polarizability of ligands coordinated to them, than the intensities of the other ED transitions.[35] The ratio of the integrated intensities of the  $^5D_0 \rightarrow {}^7F_2$  and  $^5D_0 \rightarrow {}^7F_1$  transitions, known as the asymmetry ratio  $[R_{12} = \int I(^5D_0 \rightarrow {}^7F_2) / \int I(^5D_0 \rightarrow {}^7F_1)]$ , is a sensitive indicator to extract information about the polarizability of ligands coordinated to the Eu<sup>III</sup> centers and/or the degree of symmetry of the crystallographic sites that such centers occupy within a lattice. [35,36] For Eu-doped LaF<sub>3</sub> phosphors, high R<sub>12</sub>

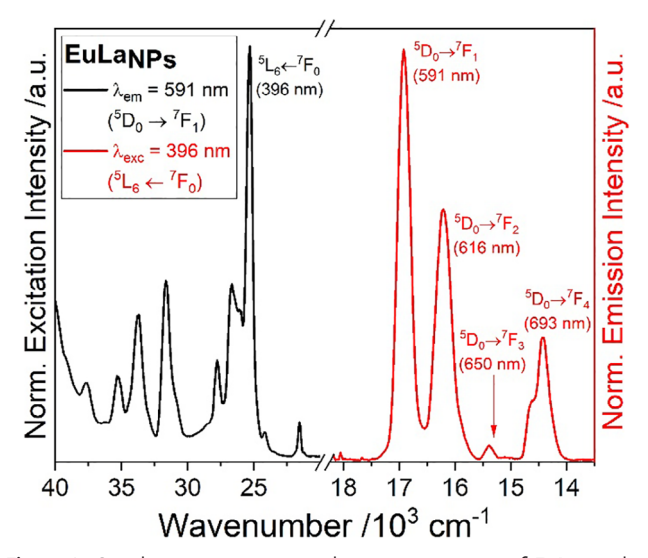


Figure 2. Steady-state excitation and emission spectra of  $EuLa_{NPs}$  dispersed in water (5 mg /3 mL).

www.advancedsciencenews.com



21951071, 0, Downloaded from https://adarced.onlinelbitary.wiley.com/doi/10.1002/ador.20250717 by Cochametalia, Wiley Online Library on [2906/2025]. See the Terms and Conditions (https://onlinelbitary.wiley.com/terms-and-conditions) on Wiley Online Library for rules of use; OA articles are governed by the applicable Creative Commons Licenses

www.advopticalmat.de

values are indicative of high ratios of asymmetric Eu<sup>III</sup> centers, that is, Eu<sup>III</sup> ions located at the surface of the particles (Eu<sub>surface</sub>), whose coordination spheres are completed by solvents, surfactants or other species present in the medium. For ultrasmall Eudoped LaF<sub>3</sub> NPs, R<sub>12</sub> values of up to 1.6 have been reported.<sup>[37]</sup> In our case, R<sub>12</sub> values of 0.75(1) and 0.67(2) were found for EuLa<sub>NPs</sub> and EuLa<sub>SMDs</sub>, respectively (Figure S5, Supporting Information). As expected, the higher specific surface area of smaller EuLa<sub>NPs</sub> compared to larger  $EuLa_{SMDs}$  implies a greater ratio of asymmetric Eu<sub>surface</sub> centers to inner Eu<sub>core</sub> centers (symmetric), which justifies the higher value of R<sub>12</sub> obtained for the small NPs. The emission spectra were also registered after application of a delay time (D.T.) of 0.1 ms. After this delay, the asymmetry ratios diminished to 0.67(2) for  $EuLa_{NPs}$  and 0.60(1) for  $EuLa_{SMDs}$ , indicating that the ED  $^5D_0 \rightarrow {}^7F_2$  transition decays faster than the MD  ${}^5D_0 \rightarrow {}^7F_1$ , as evidenced in the decay traces collected at 596 and 616 nm (vide infra).

## 2.3. Synthesis and Photophysical Properties of EuLa@Ir1 Composites

To determine the capacity of **Ir1** to function as a light-harvesting unit and to sensitize Eu-based emission in Eu-doped LaF<sub>3</sub> phosphors, first we carried out luminescence titrations by addition of successive quantities of **Ir1** to DMF suspensions of **EuLa**<sub>NPs</sub> and **EuLa**<sub>SMDs</sub> (hydrophilic DMF was selected as solvent due to the low solubility of **Ir1**, isolated in the form of hexafluorophosphate salt, in water). Following each addition, the mixture was subjected to sonication for 2 min to facilitate the coordination of **Ir1** to the surface of the particles and to prevent agglomeration. Two different excitation wavelengths were investigated: i)  $\lambda_{\rm exc}$  = 340 nm, where the absorption of **Ir1** is maximal and the absorption of Eu<sup>III</sup> centers is nearly negligible, and; ii)  $\lambda_{\rm exc}$  = 396 nm, which corresponds to the maximum of the  ${}^5L_6 \leftarrow {}^7F_0$  Eu-based absorption band, but the excitation intensity of the **Ir1** moieties at this wavelength remains significant.

Furthermore, as the average lifetimes of the Ir<sup>III</sup> and Eu<sup>III</sup> emissive species differ by more than three orders of magnitude (see below), it was possible to discern between one or another by time gating. Consequently, the emission spectra were collected in both steady-state (gate time = 1  $\mu$ s) and time-delayed (D.T. = 0.1 ms, gate time = 5 ms) modes, thereby enabling the isolation of the Ir-based and Eu-based emissions. The principal findings of the **EuLa<sub>NPs</sub>** titration are presented in **Figure 3**.

The addition of **Ir1** resulted in a gradual increase in the time-delayed Eu-based emission, irrespective of the excitation wavelength considered (Figure 3a–c). As shown in Figure 3a,b, the intensity of the time-delayed Eu-based emission exhibited a pronounced increase at the outset of the titration. This behavior is consistent with a strong surface chelating capacity of **Ir1** and efficient Eu<sup>III</sup> photosensitization. The photosensitization process was particularly efficient at  $\lambda_{\rm exc} = 340$  nm, where the absorption of **Ir1** is at its maximum. The integrated emission intensities of the  $^5D_0 \rightarrow ^7F_{1,2}$  bands reached a maximum when  $\approx 4.5 \cdot 10^{-8}$  mol of **Ir1** per gram of **EuLa**<sub>NPs</sub> were added (Figure 3c). Based on the assumption that the **EuLa**<sub>NPs</sub> nanoparticles can be considered spheres with a mean diameter of 35.5 nm (TEM), and that each **Ir1** complex occupies a surface area of  $\approx 1.1$  nm<sup>2</sup>, we estimated a

ratio of  $\approx 4.10^3$  molecules of Ir1 per single EuLa<sub>NPs</sub> nanoparticle, indicating full coverage of the surface area of the NPs by the Ir1 complexes (see SI, section 3 for further details). At this point of the titration, the integrated intensity of the MD  $^5D_0 \rightarrow ^7F_1$  band exhibited an increase of  $\approx$ 70-fold ( $\lambda_{\rm exc}$  = 340 nm) and tenfold ( $\lambda_{\rm exc}$ = 396 nm) compared to that of pristine **Eula<sub>NPs</sub>**. The integrated intensity of the ED  $^5D_0 \rightarrow {}^7F_2$  band showed an even more pronounced increase, reaching  $\approx$ 76 ( $\lambda_{\rm exc}$  = 340 nm) and  $\approx$ 12 ( $\lambda_{\rm exc}$  = 396 nm) times the initial intensity before the addition of Ir1. The further enhancement in intensity of the ED-band over the MDband resulted in an increase of the asymmetry ratio, from  $R_{12}$  = 0.67(2) for bare NPs to a mean value of  $R_{12} \approx 0.84$  after Ir1 functionalization (Figure 3d). Throughout the titration, excitation of the Ir1 moieties at  $\lambda_{\rm exc}$  = 340 nm resulted in an Eu-based emission that was  $\approx$ 2.4 times more intense than that observed at  $\lambda_{\rm evc}$ = 396 nm. These titration experiments demonstrate the ability of Ir1 to sensitize Eu-based emission through Ir  $\rightarrow$  Eu EnT. It is noteworthy that when an excess of Ir1 was added, the Eu-based emission intensity slightly decreased. This may be due to an inner filter effect generated by the high concentration of Ir1.

Further evidence for the existence of  $Ir \rightarrow Eu EnT$  was provided by monitoring the time-delayed Eu-based excitation spectra ( $\lambda_{\mathrm{em}}$ = 591 nm,  ${}^5D_0 \rightarrow {}^7F_1$ ) after the addition of Ir1 aliquots. The observed profiles (Figure 3e), exhibited a striking similarity to the Ir-based excitation spectrum of La<sub>NPs</sub>@Ir1 (Figure 1b). Although the Eu-based excitation band  ${}^{5}L_{6} \leftarrow {}^{7}F_{0}$  ( $\lambda_{\rm exc} = 396$  nm) was initially discernible (marked with an asterisk in Figure 3e), it was rapidly obscured by the broad and intense Ir1 excitation bands as its concentration increased. Generally, the double-electron exchange mechanism (Dexter-type) is presumed to be the predominant mechanism in  $Ir \rightarrow Eu$  energy transfer (EnT) processes. Nevertheless, dipole-dipole (Förster-type) or higher-order multipolar mechanisms may also be involved in the EnT process, given the proximity of the excited state of Ir1, localized on the anchoring dcbpy unit, to the nanoparticle surface. Irrespective of the Ir  $\rightarrow$  Eu EnT mechanism under consideration, it is assumed that the efficiency of such a process decreases as the distance between the energy donor (Ir) and energy acceptor (Eu) increases. Therefore, the Eu<sup>III</sup> centers situated on the surface of the nanoparticle and directly coordinated to Ir1 (Dexter mechanism) and those located in very close proximity and influenced by the polarizability of Ir1 (if dipole-dipole or multipolar EnT occurs) will be preferentially sensitized, which can explain the increase of the R<sub>12</sub> value observed throughout the titration. The fact that an identical  $R_{12}$ value was found regardless of the excitation wavelength considered indicates that the Eu-based emission in EuLa<sub>NPs</sub>@Ir1 originates essentially from Eu<sub>surface</sub> centers through non-radiative Ir  $\rightarrow$ Eu<sub>surface</sub> EnT. The intrinsic high surface-to-volume ratio of these small NPs results in a high concentration of Ir1, whose intense excitation bands obscure those of the Eu<sup>III</sup> centers (essentially the  ${}^{5}L_{6} \leftarrow {}^{7}F_{0}$  band centered at 396 nm), through which excitation of Eu<sub>core</sub> centers could be otherwise achieved.

Finally, the steady-state emission spectra (Figure 3f) showed the characteristic Ir-based yellow emission, which increased in intensity with successive additions of Ir1. This increase is certainly due to the formation of Ir – La $_{\rm surface}$  pairs, where EnT is not possible, and it may also arise from Ir – Eu $_{\rm surface}$  pairs if we assume that the efficiency of the Ir  $\rightarrow$  Eu energy transfer is not complete.

21951071, 0, Downloaded from https://advanced.onlinelibrary.wiley.com/doi/10.1002/adom.202500717 by Cochraneltalia, Wiley Online Library on [29/06/2025]. See the Terms

and-conditions) on Wiley Online Library for rules of use; OA articles are governed by the applicable Creative Commons License

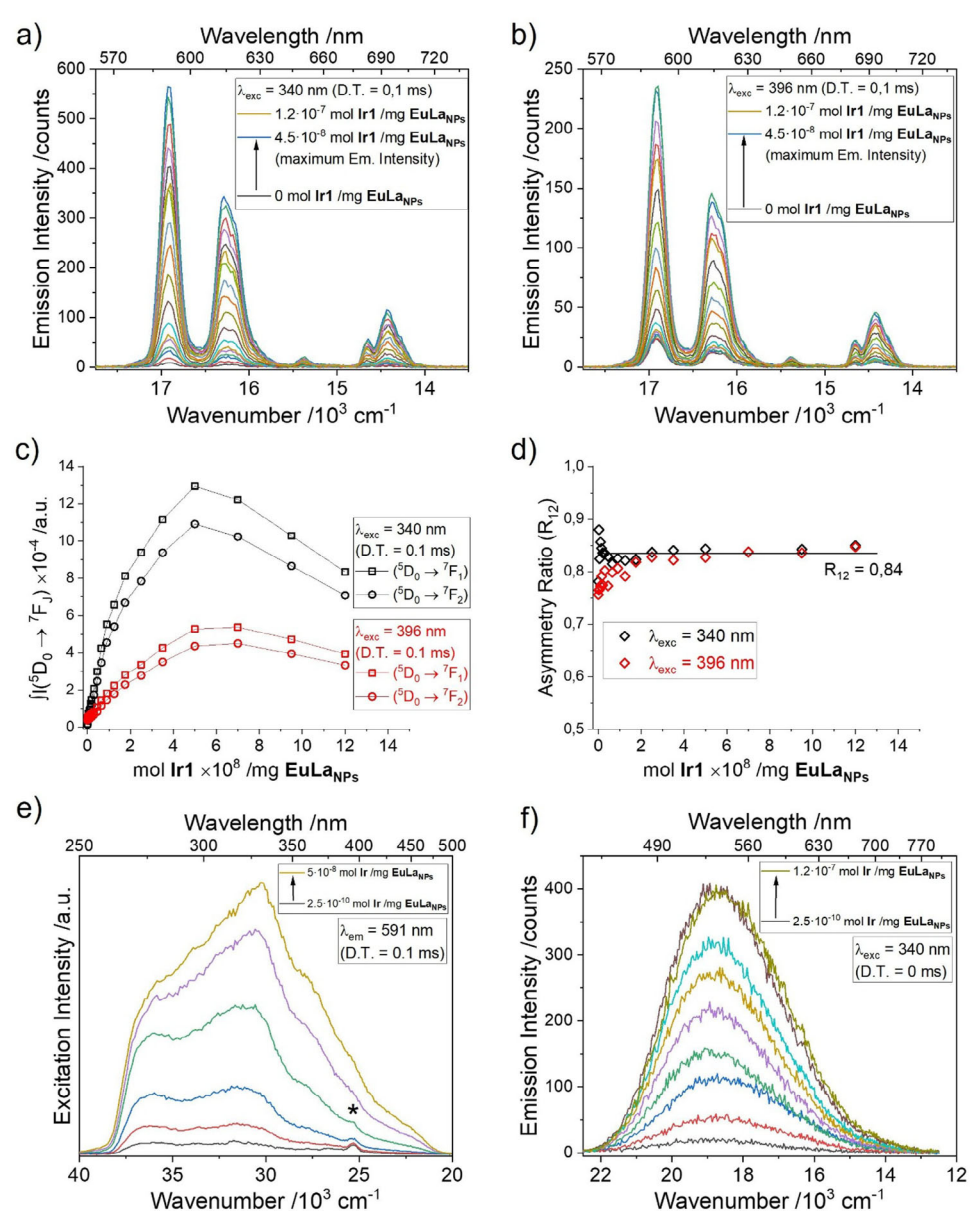


Figure 3. For EuLa<sub>NPs</sub>: Variation of the time-delayed (D. T. = 0.1 ms) Eu-based luminescence spectra with added Ir1 under excitation at  $\lambda_{exc} = 340$  nm (a) and 396 nm (b). c) Variation of the integrated intensities of the  ${}^5D_0 \rightarrow {}^7F_1$  (squares) and  ${}^5D_0 \rightarrow {}^7F_2$  (circles) Eu-bands with added Ir1 under excitation at  $\lambda_{exc} = 340$  nm (black) and 396 nm (red). d) Variation of the asymmetry ratio (R<sub>12</sub>) with added Ir1 under excitation at  $\lambda_{exc} = 340$  nm (black) and 396 nm (red diamonds). e) Variation of the time delayed (D. T. = 0.1 ms) Eu-based excitation spectra ( $\lambda_{em} = 591$  nm,  ${}^5D_0 \rightarrow {}^7F_1$  band) with added Ir1 (asterisk indicates direct excitation of Eu<sup>III</sup> centers). f) Variation of the steady-state Ir-based luminescence spectra (gate time = 1 μs) with added Ir1 under excitation at  $\lambda_{exc} = 340$  nm. The titration was carried out in DMF at room temperature.

Many of the comments made above also apply to  $EuLa_{SMDs}$  titration (Figure S6, Supporting Information), although some peculiarities need to be noted. The Eu-based emission of  $EuLa_{SMDs}$  is clearly enhanced after the addition of Ir1 (Figure S6a,b, Supporting Information), although this increase was modest compared to that observed for the small NPs. The maximum of the Eu-based emission was reached at a concentration of about  $6\cdot10^{-9}$  mol of Ir1 /mg  $EuLa_{SMDs}$ , which allowed us to calculate a ratio of about  $1.34\cdot10^5$  molecules of Ir1 per submicron disk (Section 3.2, SI) and about 74% of the particle surface occupied by the  $Ir^{III}$  complexes. It is noteworthy that this optimal Ir1 concen-

tration is nearly one order of magnitude lower than that found for  $\text{EuLa}_{\text{NPs}}$ , which serves to confirm that the specific surface area of the particles decreases as their size increases. At this point of the titration, the integrated intensities of the  $^5D_0 \rightarrow ^7F_J$  bands at  $\lambda_{\text{exc}}=396$  nm exhibited an  $\approx 2.2\text{-fold}$  and 3.2-fold increase for J = 1 and J = 2, respectively. At  $\lambda_{\text{exc}}=340$  nm, before the addition of Ir1, the Eu-based emission was undetectable, thereby precluding the calculation of the net increase in intensity of the  $^5D_0 \rightarrow ^7F_{1,2}$  bands during the titration. Such emission could only be reliably detected after the initial addition of 2.5·10 $^{-10}$  mol Ir1 /mg  $\text{EuLa}_{\text{SMDs}}$ . At the optimal point of the titration, the

ADVANCED
OPTICAL
MATERIALS

Downloaded from https://advanced.onlinelibrary.wiley.com/doi/10.1002/adom.202500717 by Cochraneltalia, Wiley Online Library on [2906/2025]. See the Terms and Conditions (https://onlinelibrary.wiley.com/terms-and-conditions) on Wiley Online Library for rules of use; OA articles are governed by the applicable Creative Commons Licenses

emission intensity was  $\approx$ 8.5 times higher than that observed initially.

The changes observed in R<sub>12</sub> as a function of added Ir1 are in this case of particular interest. At  $\lambda_{\rm exc} = 340$  nm, an almost constant value of  $R_{12} \approx 1.15$  was found throughout the titration. This high value indicates that Eu<sub>surface</sub> centers located nearby Ir1 moieties are preferentially sensitized through Ir  $\rightarrow$  Eu EnT. At  $\lambda_{\rm exc}$  = 396 nm, the  $R_{12}$  value increased from  $R_{12} = 0.65(2)$  (bare submicron disks) to a mean value of  $R_{12} \approx 0.97$  following the addition of the optimal amount of Ir1, and then remained constant until the end of the titration (Figure S6d, Supporting Information). Such an increase supports preferential Ir1-photosensitization of Eu<sub>surface</sub> centers, although the fact that its value is lower than that found under excitation at  $\lambda_{\rm exc}$  = 340 nm, is indicative of a significant contribution of symmetric Eu<sub>core</sub> centers to the global Eu-based emission. The excitation spectra profiles registered at  $\lambda_{\rm em}$  = 591 nm (MD  $^5D_0 \leftarrow {}^7F_1$  band) after successive additions of Ir<sup>III</sup> aliquots (Figure S6e, Supporting Information) showed an increasing resemblance to that of Ir1, confirming the existence of non-radiative Ir  $\rightarrow$  Eu energy transfer. However, the Eubased  ${}^{5}L_{6} \leftarrow {}^{7}F_{0}$  excitation peak at 396 nm (marked with an asterisk) was consistently discernible regardless of the amount of **Ir1** added. This evidence corroborates the hypothesis that at  $\lambda_{\text{exc}}$ = 396 nm, both Ir1-sensitized  $Eu_{surface}$  and directly excited  $Eu_{core}$ centers contribute to the global Eu<sup>III</sup> emission and justifies the intermediate value of  $R_{12} = 0.97$  found.

After the titration experiments, we proceed to isolate EuLa<sub>NPs</sub>@Ir1 and EuLa<sub>SMDs</sub>@Ir1 composites. The solids were prepared by mixing the respective bare particles suspended in CH3Cl with an excess of Ir1 dissolved in the same solvent (see SI, section 1). It should be noted that the amount of Ir1 loaded to functionalize the surface of the particles was slightly higher than the optimal amount calculated from the titration experiments. This was done to ensure full coverage of the particles' surfaces. Following surface functionalization, the size and morphology of the composite particles remained similar to that of the originals materials. The attachment of Ir1 to the surface of the particles was confirmed by transmission electron microscopy coupled with energy-dispersive X-ray spectroscopy (TEM-EDX, Figure \$7, Supporting Information), infrared spectroscopy (IR, Figure S8, Supporting Information) and X-Ray photoelectron spectroscopy (XPS, Figures S9 and S10, Supporting Information). The XPS spectra of both composites exhibit the expected 3d and 4d photoemissive lines of La (3d peaks at 835.1 and 852.0 eV and 4d peaks at 102. and 105.8 eV) and Eu (3d main peak at 1130.5 eV and 4d at 136.3 eV) ions. The distinctive 4f Ir peaks  $(4f_{5/2} \text{ and } 4f_{7/2} \text{ peaks at } 64.0 \text{ and } 61.0 \text{ eV}, \text{ respectively})$  were also discernible.

To determine the influence of **Ir1** on the Eu<sup>III</sup> -based emission in these d-f hybrid materials, we also recorded the emission properties of bare **EuLa<sub>NPs</sub>** and **EuLa<sub>SMDs</sub>** and their respective **Ir1** composites in the solid state (Figures S11–S13, Supporting Information). The integrated emission intensity of the MD  $^5D_0 \rightarrow ^7F_1$  band in the **EuLa<sub>NPs</sub>@Ir1** composite increased 41-, 44-, 2-, and 188-fold upon excitation at  $\lambda_{\rm exc} = 273$ , 340, 396, and 430 nm, respectively (Figure S11, Supporting Information). Additionally, the asymmetry ratio increased from R<sub>12</sub> = 0.69(2) to 0.85(2) (Figure S12, Supporting Information). Therefore, the amplifying effect of **Ir1** on the Eu-based emission of **EuLa<sub>NPs</sub>@Ir1** 

and the preferential sensitization of  $\rm Eu_{surface}$  centers are also evident in the solid state.

The solid  $EuLa_{SMDs}$ @Ir1 exhibited a comparable amplification effect, with the integrated emission of the MD Eu-band increasing by factors of 29-, 126-, and 307- compared to bare submicron disks after preferential excitation of Ir1 at  $\lambda_{exc}=273$ , 340, and 430 nm, respectively (Figure S11, Supporting Information). The asymmetry ratio increased for  $R_{12}=0.60(1)$  (for  $EuLa_{SMDs}$  at  $\lambda_{exc}=396$  nm) until  $R_{12}\approx0.91(2)$  (Figure S13c–e, Supporting Information). It is noteworthy that, at  $\lambda_{exc}=396$  nm, the Eu-based emission intensity of the composite increased by a factor of 2.5 and an intermediate asymmetry ratio of  $R_{12}=0.81(2)$  was calculated (Figure S13b, Supporting Information). This further confirms that for  $EuLa_{SMDs}$ @Ir1, this excitation wavelength promotes both emission from Ir1-sensitized  $Eu_{surface}$  centers and from directly excited  $Eu_{core}$  centers.

In order to quantify the ratio of  $Eu_{surface}/Eu_{core}$  emissive centers in  $EuLa_{NPs}$  and  $EuLa_{SMDs}$  and in the respective hybrids, we analyzed the decay of the  $^5D_0 \rightarrow ^7F_{1,2}$  transitions over time after excitation at  $\lambda_{exc} = 396$  nm (for pristine and composite samples) and  $\lambda_{exc} = 430$  nm (for composites). These two excitation wavelengths were selected based on their ability to elicit the most pronounced differences in Eu-based emission intensity between the composites and pristine particles.

For Eu-doped LaF<sub>3</sub> phosphors, the Eu-based  $^5D_0$  excited state lifetime is usually given by equation 1:

$$1/\tau = W_{0-1} + W_{0-2} \tag{1}$$

Where  $W_{0-1}$  and  $W_{0-2}$  are the magnetic ( ${}^5D_0 \to {}^7F_1$ ) and electric ( ${}^5D_0 \to {}^7F_1$ ) transition probabilities, respectively [the contribution of other  ${}^5D_0 \to {}^7F_1$ ) ( $J=0,\ 3-6$ ) transition probabilities and the existence of Eu – Eu interionic interactions were in first instance considered negligible]. As noted before,  $W_{0-1}$  is almost insensitive to the geometry of the coordination sphere around the Eu<sup>III</sup> ion and its value can be considered constant. By contrast, low symmetry environments around Eu<sup>III</sup> sites enables  $W_{0-2}$  to be enhanced and, thereby reducing the lifetime of the  ${}^5D_0$  emissive state (as outlined in equation 1). Assuming a model with two Eu<sup>III</sup> sites, centrosymmetric Eu<sub>core</sub> and low symmetry Eu<sub>surface</sub> centers, a correlation between short  ${}^5D_0$  lifetimes and large Eu<sub>surface</sub>/Eu<sub>core</sub> ratios can be established. The  ${}^5D_0$  emission decay curves (**Figure 4**) were fitted to a double exponential function according to equation 2:

$$I(t) = I_0(t) + \alpha e^{\left(-t/\tau_f\right)} + \beta e^{\left(-t/\tau_s\right)}$$
 (2)

Where  $\tau_f$  and  $\tau_s$  represent the times associated with the fast and slow decay components, and  $\alpha$  and  $\beta$  denote the respective amplitude ratios ( $\alpha + \beta = 1$ ). The corresponding fitting parameters are summarized in **Table 1**, together with the average decay times ( $\tau_{au}$ ), defined as follows:

$$\tau_{av} = \frac{\int_{t_0}^{t_f} tI(t)}{\int_{t_0}^{t_f} I(t)} = \frac{\left(\alpha \cdot \tau_f^2 + \beta \cdot \tau_s^2\right)}{\left(\alpha \cdot \tau_f + \beta \cdot \tau_s\right)}$$
(3)

In general, the  $\tau_{av}$  values extracted for the  $^5D_0 \rightarrow {}^7F_{1,2}$  decays are shorter for **EuLa**<sub>NPs</sub> and **EuLa**<sub>NPs</sub>@**Ir1** than those calculated

21951071, 0, Downloaded from https://advanced.onlinelibrary.wiley.com/doi/10.1002/adom.202500717 by Cochraneltalia, Wiley Online Library on [29/06/2025]. See the Terms and Conditions (https://onlinelibrary.wiley.com/doi/10.1002/adom.202500717 by Cochraneltalia, Wiley Online Library on [29/06/2025]. See the Terms and Conditions (https://onlinelibrary.wiley.com/doi/10.1002/adom.202500717 by Cochraneltalia, Wiley Online Library on [29/06/2025]. See the Terms and Conditions (https://onlinelibrary.wiley.com/doi/10.1002/adom.202500717 by Cochraneltalia, Wiley Online Library on [29/06/2025]. See the Terms and Conditions (https://onlinelibrary.wiley.com/doi/10.1002/adom.202500717 by Cochraneltalia, Wiley Online Library on [29/06/2025]. See the Terms and Conditions (https://onlinelibrary.wiley.com/doi/10.1002/adom.202500717 by Cochraneltalia, Wiley Online Library on [29/06/2025]. See the Terms and Conditions (https://onlinelibrary.wiley.com/doi/10.1002/adom.202500717 by Cochraneltalia, Wiley Online Library on [29/06/2025]. See the Terms and Conditions (https://onlinelibrary.wiley.com/doi/10.1002/adom.202500717 by Cochraneltalia, Wiley Online Library on [29/06/2025]. See the Terms and Conditions (https://onlinelibrary.wiley.com/doi/10.1002/adom.202500717 by Cochraneltalia, Wiley Online Library on [29/06/2025]. See the Terms and Conditions (https://onlinelibrary.wiley.com/doi/10.1002/adom.202500717 by Cochraneltalia, Wiley Online Library.wiley.com/doi/10.1002/adom.2025007 by Cochraneltalia, Wiley Online Library.wiley.wiley.com/doi/10.1002/adom.2025007 by Cochraneltalia, Wiley Onli

and-conditions) on Wiley Online Library for rules of use; OA articles are governed by the applicable Creative Commons License

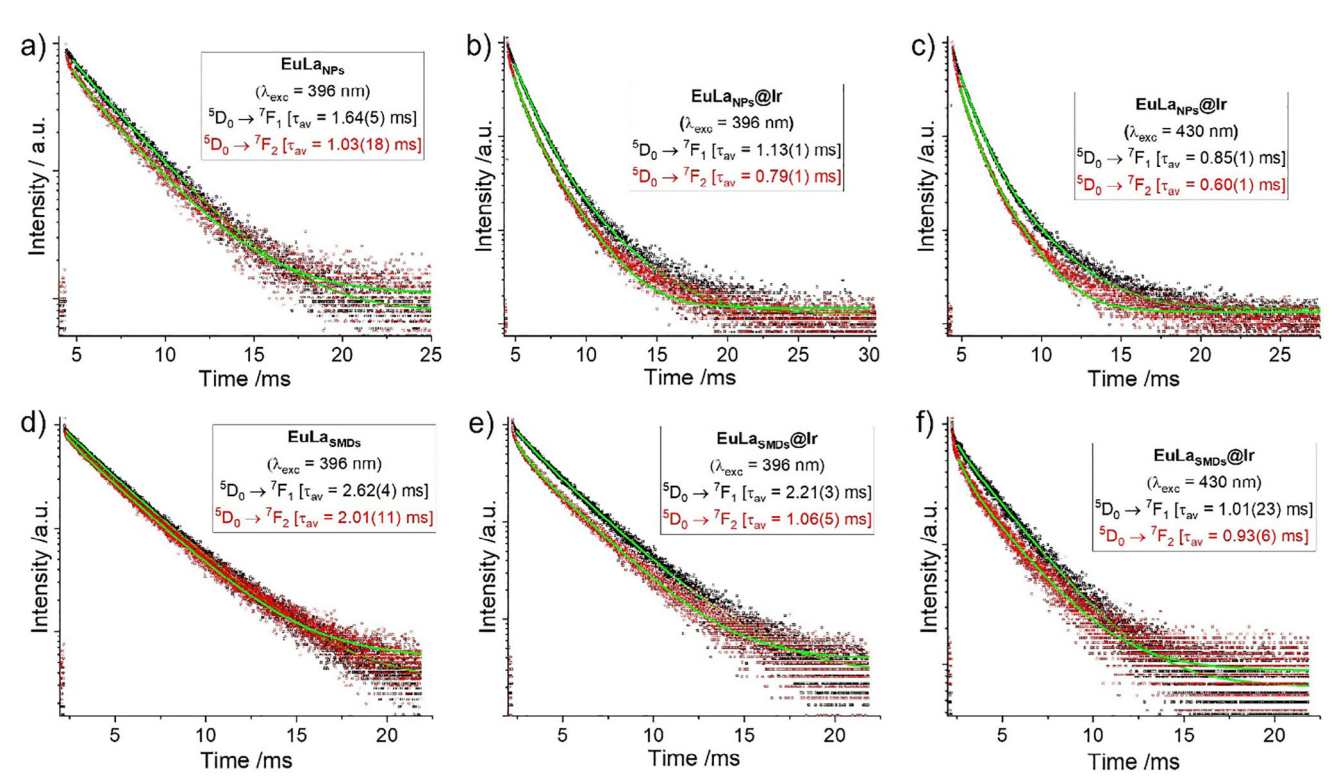


Figure 4. Decay curves for  ${}^5D_0 \to {}^7F_1$  (black squares) and  ${}^5D_0 \to {}^7F_2$  (red squares) emissions of a) **EuLa<sub>NPs</sub>**, b,c) **EuLa<sub>NPs</sub>@Ir1**, d) **EuLa<sub>SMDs</sub>** and e,f) **EuLa<sub>SMDs</sub>@Ir1** dispersed in water (5 mg /3 mL).

for the respective **EuLa<sub>SMDs</sub>** and **EuLa<sub>SMDs</sub>@Ir1**, confirming that the ratio of short-lived Eu<sub>surface</sub> emitters increases as the size of the particles decreases.

The products  $(\alpha \cdot \tau_f)$  and  $(\beta \cdot \tau_s)$  from equation 2 are significantly correlated with the number of Eu<sub>surface</sub> and Eu<sub>core</sub> centers present within the particles. Thus, the Eu<sub>surface</sub>/Eu<sub>core</sub> ra-

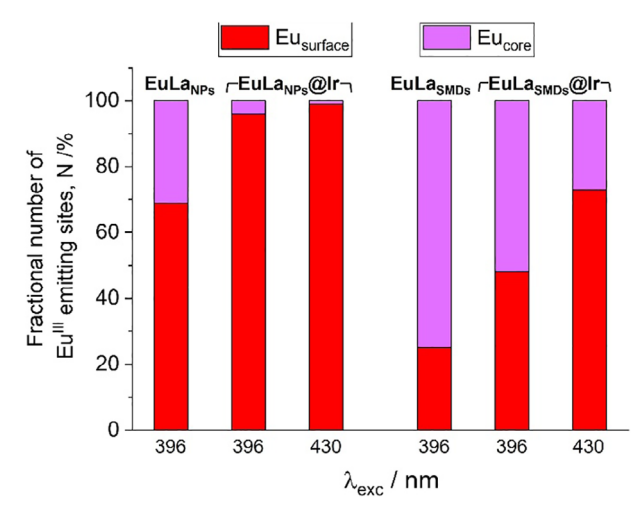
tio can be estimated quantitatively using the data extracted from the decay curves analysis and a straightforward analytical method proposed by Hayakawa et al., [38,39] which is based on the theory of transition probabilities (see SI, section 4, for further details). Table 1 presents the fractional numbers of emitting  $Eu^{\rm III}$  centers distributed at the surface and the core

Table 1. Summary data of the  $^5D_0$  decay lifetime analysis of EuLa<sub>NPs</sub> and EuLa<sub>SMDs</sub> ( $\lambda_{\rm exc}=396$  nm) and the respective composites EuLa<sub>NPs</sub>@Ir1 and EuLa<sub>SMDs</sub>@Ir1 ( $\lambda_{\rm exc}=396$  and 430 nm) (experiments performed on water dispersions of the particles, 5 mg /3 mL).

	$^{5}D_{0} \rightarrow {}^{7}F_{J}$ peak	$ au_{ m av}$ /ms	Fast decay		Slow decay		Fraction [%]of Eu <sub>Surface</sub> /Eu <sub>core</sub> emitting ions <sup>a)</sup>
			α	$ au_{\mathrm{f}}$ /ms	β	$ au_{\rm s}$ /ms	-
EuLa <sub>NPs</sub> $(\lambda_{\text{exc}} = 396 \text{ nm}, R_{12} = 0.67)$	0 – 1	1.64(5)	0.84(15)	0.79(16)	0.16(2)	2.83(2)	69/31
	0 – 2	1.03 (18)	0.95(3)	0.71(9)	0.05(3)	2.79(3)	
EuLa <sub>NPs</sub> @Irl $(\lambda_{exc} = 396 \text{ nm}, R_{12} = 0.84)$	0 – 1	1.13(1)	0.98(1)	1.08(1)	0.02(1)	2.70(8)	96/4
	0 – 2	0.79(1)	0.99(1)	0.75(1)	0.01(1)	1.90(2)	
EuLa <sub>NPs</sub> @Ir1 $(\lambda_{\text{exc}} = 430 \text{ nm}, R_{12} = 0.84)$	0 – 1	0.85(1)	0.995(1)	0.83(1)	0.005(1)	2.29(4)	99/1
	0 – 2	0.60(1)	0.997(1)	0.59(1)	0.003(1)	1.55(2)	
EuLa <sub>SMDs</sub> ( $\lambda_{exc} = 396 \text{ nm}, R_{12} = 0.6$ )	0 – 1	2.62(4)	0.33(2)	1.46(11)	0.67(2)	2.91(4)	25/75
	0 – 2	2.01(11)	0.69(5)	0.60(4)	0.31(5)	2.72(1)	
EuLa <sub>SMDs</sub> @Ir1 $(\lambda_{exc} = 396 \text{ nm}, R_{12} = 0.81)$	0 – 1	2.21(3)	0.48(1)	1.18(7)	0.52(1)	2.63(3)	48/52
	0 – 2	1.06(5)	0.92(1)	0.53(1)	0.08(1)	2.42(1)	
EuLa <sub>SMDs</sub> @Ir1 $(\lambda_{exc} = 430 \text{ nm}, R_{12} = 0.92)$	0 – 1	1.01(23)	0.92(4)	0.44(5)	0.078(41)	2.31(1)	73/27
	0 – 2	0.93(6)	0.94(12)	0.54(3)	0.063(12)	2.30(3)	

a) Estimated using equations \$1-\$9 (see \$1, section 4).

21951071, 0, Downloaded from https://adarced.onlinelbitary.wiley.com/doi/10.1002/ador.20250717 by Cochametalia, Wiley Online Library on [2906/2025]. See the Terms and Conditions (https://onlinelbitary.wiley.com/terms-and-conditions) on Wiley Online Library for rules of use; OA articles are governed by the applicable Creative Commons Licenses



**Figure 5.** Fractional number of emitting  $Eu_{surface}$  (red) and  $Eu_{core}$  (magenta) sites for the samples studied in this work as a function of the excitation wavelength.

sites within the particle for each sample. For bare  $EuLa_{NPs}$  the emission decay after direct excitation of the  $Eu^{III}$  centers ( $\lambda_{exc}=396$  nm) is dominated by the fast decay components ( $\alpha>0.8$  and  $\tau_f<0.8$  ms) attributed to  $Eu_{surface}$  centers and a  $Eu_{surface}/Eu_{core}$  ratio of 69/31 was found. For  $EuLa_{SMDs}$ , the ratio found was  $Eu_{surface}/Eu_{core}=25/75$ , confirming that the proportion of inner  $Eu_{core}$  centers increases as does the particle size.

For  $EuLa_{NPs}$ @Ir1, regardless of the excitation wavelength considered, the short decay components were clearly dominant ( $\alpha > 0.98$ ) as the emission arose almost exclusively from  $Eu_{surface}$  centers (>95%) following Ir1 sensitization. Finally, when  $EuLa_{SMDs}$ @Ir1 was excited at  $\lambda_{exc} = 396$  nm, both  $Eu_{surface}$  and  $Eu_{core}$  centers contributed almost equally (fraction of  $Eu_{surface}/Eu_{core}$  emitting centers = 48/52) to the resulting emission. Conversely, the emission from the  $Eu_{surface}$  centers was dominant (73%) when the Ir1 moiety was preferentially excited at  $\lambda_{exc} = 430$  nm. Figure 5 illustrates the fraction of  $Eu^{III}$  emitting centers located at different sites for each sample as a function of the excitation wavelength.

Therefore, the size of the particles plays a significant role in both the nature of the emitting Eu<sup>III</sup> centers (Eu<sub>surface</sub> versus Eu<sub>core</sub>) and the different pathways through which those centers can be excited (Scheme 1). For small EuLa<sub>NPs</sub>@Ir1, the high concentration of Ir1, the high Eu<sub>surface</sub>/Eu<sub>core</sub> ratio, and consequently, the high probability of creating coordinated Ir- $Eu_{surface}$ pairs which favor non-radiative Ir  $\rightarrow$  Eu EnT, result in an Eubased emission that, regardless of the excitation wavelength considered, essentially arises from Eu<sub>surface</sub> centers through Ir1 sensitization. In contrast, for larger EuLa<sub>SMDs</sub>@Ir1 with a lower concentration of Ir1, a lower Eu<sub>surface</sub>/Eu<sub>core</sub> ratio, and consequently, a lower number of Ir - Eu pairs, preferential irradiation of Ir1  $(\lambda_{\rm exc} = 273 \text{ nm}, 340 \text{ nm} \text{ or } 430 \text{ nm})$  results in dominant sensitized Eu<sub>surface</sub> emission, whereas irradiation at  $\lambda_{exc}$  = 396 nm promotes both direct Eu<sub>core</sub> excitation and Ir1-mediated Eu<sub>surface</sub> sensitization.

#### 2.4. TG-, PLIM, and Cell Staining of EuLa@Ir1 Composites

Given the extraordinary luminescent features of the hybrid EuLa@Ir1 composites, to ascertain their utilization in advanced imaging and biomedical applications, we employed TG-imaging and PLIM microscopy to image the loading of the nanocomposites in model HEK-293 cell cultures. This cell line is frequently employed in biocompatibility and nanotoxicity assays.

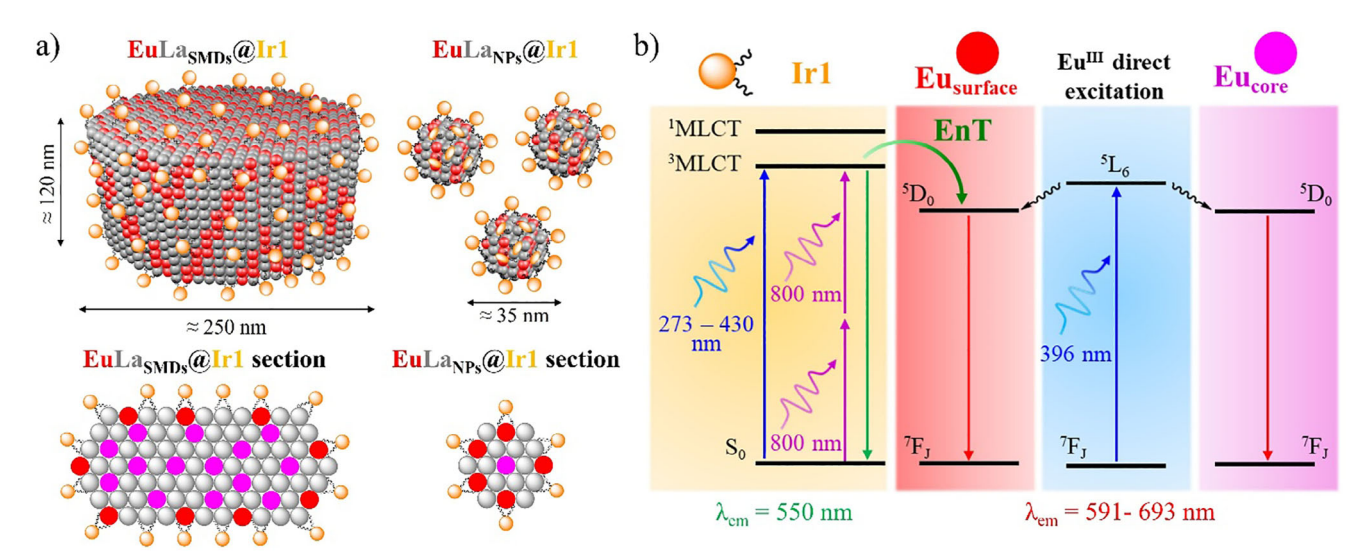
First, we investigated the stability of both composites in aqueous, hydrophilic and serum-supplemented biological media (Dulbecco's Modified Eagle's Medium, cDMEM). To assess the ability of Ir1 to remain coordinated to the particles' surface in these media, dispersions of EuLa<sub>NPs</sub>@Ir1 and EuLa<sub>SMDs</sub>@Ir1 were subjected to dialysis in water, DMF and cDMEM for a period of 5 days. The UV-vis spectra of the dialysis solvents were recorded at 24-h intervals. During this period, the characteristic absorption bands of Ir1 were not detected, which allowed us to conclude that there was no leakage of Ir1. However, during this period, the particles suspended in water gradually settle at the base of the dialysis bag, indicating a tendency of these hybrids to precipitate in this medium. This tendency was particularly apparent in the case of large EuLa<sub>SMDs</sub>@Ir1 particles. Following the completion of the dialysis experiments, both types of particles were recovered, washed and redispersed in water. In both cases, the photophysical performance was comparable to that of freshly prepared samples. This confirmed the stability of these systems.

Additional evidence of aggregation was obtained through Dynamic Light Scattering (DLS) analyses. For the DLS studies, **EuLa<sub>NPs</sub>**@Ir1 and EuLa<sub>SMDs</sub>@Ir1 were diluted in Milli-Q water, PBS, serum-free DMEM, and cDMEM. Hydrodynamic diameters were measured at time 0, and after 24 and 48 h of incubation. For EuLa<sub>NPs</sub>@Ir1, due to the high polydispersity of the sample in Milli-Q water, PBS, and serum-free DMEM across all time points, the DLS measurements were of low quality (as indicated by the instrument's quality reports) and are therefore not shown. In contrast, when the nanoparticles were dispersed in cD-MEM (DMEM supplemented with 10% FBS), a hydrodynamic diameter of  $33 \pm 5$  nm was detected after 24 h, suggesting good colloidal stability (the peak at 7.9  $\pm$  1.4 nm is related to serum proteins) (Figure S14a, Supporting Information). However, after 48 h, a new peak appeared (106  $\pm$  26 nm), indicating the onset of aggregation (Figure \$14b, Supporting Information). Probably, the adsorption of proteins onto the nanoparticle surfaces likely contributed to colloidal stability by forming a hydration layer.

In the case of EuLa<sub>SMDs</sub>@Ir1, regardless of the media under consideration, DLS measurements did not provide hydrodynamic peaks corresponding to the real size of the particles, as observed by TEM, suggesting a higher tendency for these particles to aggregate. However, it is important to note that DLS assumes spherical particles for hydrodynamic diameter calculations. Therefore, the anisotropic shape of these submicron disks may also lead to inaccuracies.

Nevertheless, despite their limited dispersibility,  $EuLa_{NPs}$ @Ir1 and  $EuLa_{SMDs}$ @Ir1 were added (50  $\mu g$  mL $^{-1}$ ) to the cell culture media and imaged after 24 h under standard culture conditions. Prior to imaging, cells were treated with CellMask Green to

21951071, 0, Downloaded from https://adarced.onlinelbitary.wiley.com/doi/10.1002/ador.20250717 by Cochametalia, Wiley Online Library on [2906/2025]. See the Terms and Conditions (https://onlinelbitary.wiley.com/terms-and-conditions) on Wiley Online Library for rules of use; OA articles are governed by the applicable Creative Commons Licenses



**Scheme 1.** a) Schematic models of  $EuLa_{SMDs}@Ir1$  and  $EuLa_{NPs}@Ir1$  (top) and their respective particle's sections (bottom) where the photoactive  $Ir^{III}$  (orange),  $Eu_{core}$  (magenta) and  $Eu_{surface}$  (red) centers are distinguishable [La<sup>III</sup> centers are drawn in grey]. b) Simplified Jablonski diagram which illustrates the different pathways through which  $Eu_{surface}$  (red) centers can be sensitized in hybrid EuLa@Ir1 composites.

stain cellular membranes (see experimental section). Advanced PLIM microscopy was performed by employing three simultaneous detection channels, namely for CellMask Green, for Ir1, and for EuIII PL emission, and two different photon detection time regimes, for PL lifetimes in the ns-time regime and the ms-time regime (see Figure \$15, Supporting Information and the experimental section for instrumentation details). The long PL lifetimes of Ir1 and EuIII, compared to biological fluorescent interferents, allowed to reconstruct background-free PLIM images using different analysis time windows (TG filters) (Figure \$15b, Supporting Information). The images demonstrated good internalization of both types of nanocomposites, EuLa<sub>NPs</sub>@Ir1 and EuLasmps@Ir1, that exhibited overlapped emission of both the Ir1 complex and EuIII (Figure S15c, Supporting Information). EuLa<sub>NPs</sub>@Ir1 lied closer to the cytoplasmic membrane, suggesting an endocytic internalization pathway. Indeed, size and shape are critical parameters that influence the interactions of particles with cells, including cellular uptake, biodistribution, and toxicity.[40] Smaller NPs are typically internalized more efficiently via endocytic pathways, whereas larger particles may exhibit different interaction mechanisms.[41] Although disk-shaped particles may face steric hindrances when attempting to internalize into cells due to their increased surface area, [42] that was not the case for  $EuLa_{SMDs}@Ir1$ , suggesting additional internalization pathways, as it has been reported for other disk-shaped NPs.[43]

Our instrumental setup allowed us to obtain PLIM images, quantifying PL lifetimes, of both the Ir1 complex and the Eu<sup>III</sup> emission (Figures 6a,b and S16, Supporting Information) through selection of regions of interest (ROIs) where emission from the nanosystems is detected and reconstruct the PL lifetime distributions (Figure 6c). The average PL lifetime values were  $520 \pm 90$  ns and  $870 \pm 20$  µs for Ir1 and Eu<sup>III</sup>, respectively, in EuLa<sub>NPs</sub>@Ir1, and  $460 \pm 80$  ns and  $870 \pm 30$  µs for Ir1 and Eu<sup>III</sup>, respectively, in EuLa<sub>SMDs</sub>@Ir1 (Figure 6d). The values of  $\tau_{\rm Eu}$  did not exhibit notable differences between the two types of nanosys-

tems. Considering the preferential excitation of **Ir1** (at 375 nm), so that the majority of Eu<sup>III</sup> emission comes from EnT to Eu<sub>surface</sub>, and that our optical configuration focuses on the  $^5D_0 \rightarrow ^7F_2$  band of Eu<sup>III</sup>, these  $\tau_{Eu}$  are in good agreement with those gathered in Table 1 for Eu<sub>surface</sub> preferential emission.

Finally, to assess the safe utilization of these nanocomposites in biological applications, cytotoxicity in HEK-293 cell cultures was examined across an increasing range of particle concentrations, reaching exceedingly high levels. Cells were exposed to 5, 10, 25, 50, and 100  $\mu g~mL^{-1}$  of both  $EuLa_{SMDs}@Ir1$  and  $EuLa_{NPs}Ir1$  for either 24 or 48 h, and cell viability was determined by an MTT test. The results, expressed as the percentage of viable cells, are presented in Figure 6e,f. In nanotoxicity studies, the concentrations tested typically range from low levels (1–10  $\mu g~mL^{-1}$ ) to intermediate levels (20–50  $\mu g~mL^{-1}$ ). It is unlikely that extremely high concentrations, such as 100  $\mu g~mL^{-1}$ , would be encountered in vivo. However, they are often employed to simulate extreme scenarios or to establish an upper limit for evaluating toxic effects.  $^{[44]}$ 

Following a 24-h exposure period, no notable alterations in cell viability were observed when either systems were tested at concentrations up to 50 µg mL<sup>-1</sup>. Therefore, at concentrations relevant to biomedical applications, the results indicated the absence of short-term toxicity. However, when higher concentrations of particles ( $\geq$ 50 µg mL<sup>-1</sup>) were explored, a toxic effect was observed, resulting in a reduction in cell viability by  $\approx$ 20%. This effect was observed for both types of particles. Following a 48h incubation period, EuLa<sub>SMDs</sub>@Ir1 did not result in a reduction in cell viability, indicating a recovery in the cell population. This recovery is likely due to an increased rate of cell division and a reduced toxic effect. In contrast, small EuLa<sub>NPs</sub>@Ir1 exhibited a similar response to the 24-h incubation, with a significant reduction in cell viability of up to 40% at the highest concentration studied. These differences in cell viability could be related to both the shape and the size of the investigated systems.[40]

21951071, 0, Downloaded from https://adarced.onlinelbitary.wiley.com/doi/10.1002/ador.20250717 by Cochametalia, Wiley Online Library on [2906/2025]. See the Terms and Conditions (https://onlinelbitary.wiley.com/terms-and-conditions) on Wiley Online Library for rules of use; OA articles are governed by the applicable Creative Commons Licenses

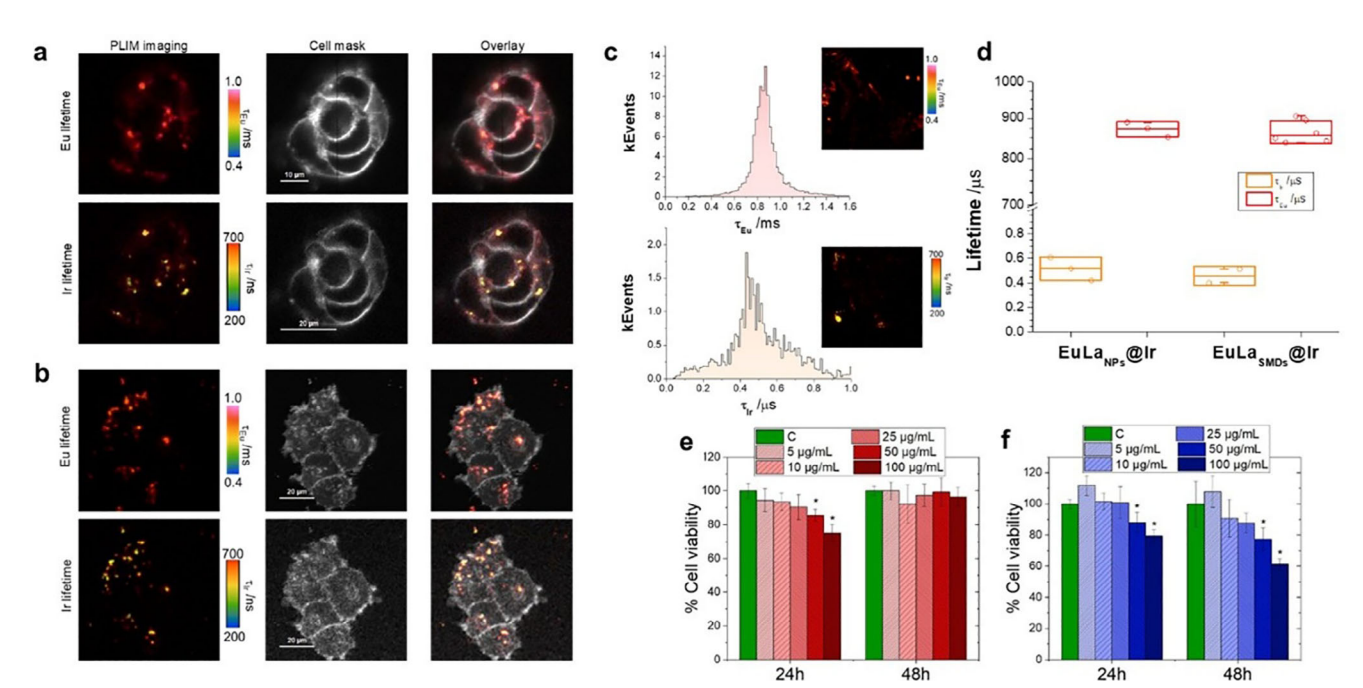


Figure 6. a,b) PLIM imaging of  $EuLa_{NPs}@Ir1$  (a) and  $EuLa_{SMDs}@Ir1$  (b) in HEK-293 cells stained with CellMask Green. The PLIM images represent the PL lifetime of  $Eu^{III}$  (630/60 nm detector, ms-time regime, TG filter > 160 µs) and the Ir1 complex PL lifetime (550/40 nm detector, ns-time regime, TG filter > 160 ns). The CellMask intensity images are depicted in gray and are reconstructed with photons collected using the TG filters 0–160 µs for the ms-time regime, or 0–160 ns for the ns-time regime. The right column represents overlaid PLIM and CellMask images. c) Representative PL lifetime distributions from Ir1 (top) and  $EuI^{III}$  (bottom) PLIM images. d) Average PL lifetimes of Ir (orange) and  $EuI^{III}$  (red) from  $EuLa_{NPs}@Ir1$  and  $EuLa_{SMDs}@Ir1$  in HEK-293 cells. e,f) Cell viability by MTT of HEK-293 cells after 24 and 48 h of incubation with  $EuLa_{SMDs}@Ir1$  (e, in red) and  $EuLa_{NPs}@Ir1$  (f, in blue). Various concentrations (5, 10, 25, 50, and 100 µg  $mL^{-1}$ ) were tested, represented by increasing color intensity. The results are expressed as mean  $\pm$  SD (standard deviation) of three independent experiments (n=3). Statically significative differences (T-student mean comparison test p<0,05) are highlighted with "\*\*."

#### 3. Conclusion

In summary, the present study demonstrates the ability of Ir<sup>III</sup>based carboxylate complexes to coordinate the surface of Eudoped lanthanide particles and sensitize Eu-based emission following Ir → Eu energy transfer. EuLa<sub>SMDs</sub>@Ir1 and EuLa<sub>NPs</sub>@Ir1 composites exhibit yellow (Ir) and amplified red (Eu) emission components, which can be generated following excitation of the transition metal at a single wavelength with energies ranging between the UV and NIR spectroscopic regions. The emission lifetimes of both components differ significantly, enabling selective detection of each through time-gated emission spectroscopy. This study further underscores the role of particle size in affecting the probability of  $Ir \rightarrow Eu$  energy transfer. For large  $EuLa_{\text{SMDs}} @Ir1$  particles, which have a low surface-to-volume ratio, a low Eu<sub>surface</sub>/Eu<sub>core</sub> ratio, and consequently a low number of coordinating Ir1-Eu<sub>surface</sub> pairs, Eu<sub>surface</sub> emission is dominant under preferential sensitization of the  $\mathrm{Ir^{III}}$  moiety. Conversely, simultaneous excitation of Ir1 and  $Eu^{\rm III}$  promotes both  $Eu_{\rm surface}$ and Eu<sub>core</sub> emissions. For smaller EuLa<sub>NPs</sub>@Ir1 nanoparticles, the high number of Ir1-Eu<sub>surface</sub> pairs enhances the probability of short-range Ir  $\rightarrow$  Eu energy transfer, and Ir-sensitized Eu<sub>surface</sub> emission is essentially detected regardless of the excitation wavelength considered.

The composites presented in this study demonstrate considerable potential for bioimaging and phototherapy applications as they combine long emission lifetimes, the possibility of NIR sen-

sitization, and good cell permeability without toxicity at concentrations typically utilized in in vitro studies. Subsequent surface modification could augment their potential for active tumor targeting, rendering them optimal candidates for theranostic systems. Future research could concentrate on the functionalization of these particles with biomolecules that target specific tumor markers and enhance dispersibility. This would facilitate both imaging and targeted therapy, thereby accelerating the clinical translation of these particles for cancer treatment.

#### 4. Experimental Section

*Materials*: Reactants and solvents were purchased from commercial suppliers and used as received without further purification unless otherwise stated.

Cell Line and Culture Conditions and Cell Viability: Human embryonic kidney cell line HEK-293 was purchased from the CIC (Centro de Instrumentación Científica) of the University of Granada, Spain. Cells were cultured in Dulbecco's Modified Eagle's Medium (DMEM; Thermo Fischer Scientific, MA, USA) supplemented with 10% (v/v) fetal bovine serum (FBS; Thermo Fischer Scientific, MA, USA) and 1% penicillin-streptomycin solution (Thermo Fischer Scientific, MA, USA). The cells were maintained at 37 °C in an incubator with 5% CO $_2$  and 95% humidity. Routine testing confirmed that the cell lines were free from mycoplasma contamination.

An MTT viability assay was performed to assess HEK-293 cell viability following NP exposure. Briefly, cells were seeded at a density of  $5\times10^3$  cells per well in 96-well plates. The cells were cultured for 24 h and then exposed to various concentrations (5, 10, 25, 50, and 100  $\mu$ g mL<sup>-1</sup>) of both **Eula<sub>SMDs</sub>@Ir1** and **Eula<sub>NPs</sub>@Ir1** for 24 h or 48 h. After the incubation

www.advopticalmat.de

period, 20  $\mu$ L of MTT reagent (CellTiter 96 AQueous One Solution Cell Proliferation Assay, Promega, USA) were added to each well, following the manufacturer's protocol. The cells were incubated at 37 °C for 2 h, and absorbance was measured at 490 nm using an Infinite M200 Nanoquant multimode microplate reader (Tecan, Switzerland).

Characterization: Elemental analyses were carried out on a Fisons-Carlo Erba analyzer model EA1108. NMR characterizations were performed on a 400 MHz (2 channels) BRUKER Nanobay Advance III and a 600 MHz (4 channels) VARIANT DIRECT DRIVE spectrometers. Electro Spray (ESI) Mass spectrometry experiments were performed on a BRUKER-AUTOFLEX mass spectrometer. X-Ray powder diffraction measurements were collected on a Bruker D8 advance diffractometer. Nanoparticles were characterized by electron microscopy using a High Resolution GEMINI-Carl Zeiss scanning electron microscope (SEM) and a LIBRA 120 PLUS Carl Zeiss transmission electron microscope (TEM) operating at 200 keV. 5 mg of the material was redispersed by sonication (30 min) in 3 mL of H<sub>2</sub>O. HAADF-STEM images and EDX analyses were recorded on a HAADF FEI TITAN G2 instrument working at an accelerating voltage of 200 kV in the scanning mode with a probe diameter of 0.5 nm. For TEM/STEM experiments, carbon reinforced copper grids (200 mesh) were submerged into suspension 50 times and then allowed to dry in air for at least 24 h. The size of the particles was determined using Image]. X-ray photoelectron spectroscopy (XPS) experiments were carried out in a Kratos Axis Ultra-DLD. All these techniques are available at the Centro de Instrumentación Científica (CIC) of the University of Granada. UV–vis spectra were recorded at  $10^{-4}~\rm M$  concentrations in HPLC grade solvents and room temperature on a SHIMADZU UV-1800 spectrometer. Steady-State and Time-delay emission and excitation spectra were measured on a Cary Eclipse spectrofluorometer. TCSPC lifetimes were measured on a UV-vis-PTI QuantaMaster 8000 spectrofluorometer equipped with a Hg-Xe pulsed lamp (0.15 Js pulse<sup>-1</sup>) and a pulsed diode light NanoLED 340L (Horiba Scientific). Photoluminescence quantum yields were measured in DCM solutions using an integrating sphere.

Two-photon excitation (TPE) luminescence spectra, time-resolved decays and PL lifetime imaging (PLIM) were carried out on a MicroTime 200 (PicoQuant GmbH) system, based on an Olympus IX71 microscope. The excitation laser was a tunable femtosecond NIR laser Chameleon Discovery NX (Coherent, Inc.), equipped with a dual pulseSelect pulse picker (APE GmbH) to control the repetition frequency for time-resolved PL measurements. The two-photon absorption (TPA) cross-section of the Ir complex was obtained using an Andor Shamrock 303i-A spectrograph, equipped with a 150 lines mm<sup>-1</sup> grating and an Andor Newton electronmultiplying CCD camera, working in full-binning vertical mode, to collect the spectra. TPA cross section calculations were performed using the relative method, and fluorescein in aqueous basic media as a reference of known TPA cross-section and fluorescence quantum yield.[1] TPA combined with photoluminescence lifetime imaging (TPA-PLIM) and spectral imaging (Figure S14d-g, Supporting Information) of nanocomposites dispersed on a microscope coverglass was performed with the excitation laser tuned at 800 nm and a repetition frequency of 80 kHz. The PL emission was detected on a hybrid PMT (PicoQuant), after passing a 550/40 nm bandpass filter that focuses on the Ir complex PL emission. Photon timetagging was performed on a MultiHarp 150 module (PicoQuant). The TPE-PLIM images were obtained by fitting pixelwise the PL decay traces to a biexponential function decay, and the intensity-weighted average lifetime was represented on a pseudocolor scale.

Photoluminescence Lifetime Imaging Microscopy in Living Cells: HEK-293 cells were seeded in 1 $\mu$ -Slide VI 0.4 ibiTreat microscopy chambers (Ibidi GmbH) at a density of 15  $\times$  103 cells/chamber. They were incubated with 50  $\mu$  mL<sup>-1</sup> of **EuLa<sub>SMDs</sub>@Ir1** and **EuLa<sub>NPs</sub>@Ir1** for 24 h under standard culture conditions. Following incubation, the cell membranes of living cells were stained with CellMask Green (Thermo Fisher Scientific) for 10 min at 37 °C. After staining, the solution was carefully removed and the cells were rinsed with phosphate-buffered saline (PBS). Finally, the cells were left in DMEM to prepare for imaging.

PLIM imaging was subsequently performed to visualize the cells and analyze the fluorescent lifetime of the internalized  $EuLa_{SMDs}@Ir1$  and  $EuLa_{NPs}@Ir1$ . It was performed using the same instrumentation de-

scribed above for TPA-PLIM but using a 375-nm pulsed diode laser as the excitation source. The laser head was controlled with a Sepia II driver (PicoQuant) that allowed working at a repetition rate of 200 kHz for Ir1 imaging. For Eu(IIII) imaging, the Sepia II driver allowed to program a train of pulses during 125 µs, followed by a detection time window of 2.875 ms when the laser was turned off. The luminescence emission was collected back through the microscope objective and filtered through the 100-µm confocal aperture. Then, a beam splitter and a 600 DCXR dichroic mirror separated the luminescence emission to three point detectors with bandpass filters of 520/35 nm (for CellMask Green), 550/40 nm (for Ir1 luminescence), and 630/60 nm (for Eu(III) luminescence) (see Figure S3a, Supporting Information for the instrumental setup). The emitted photons were temporally and spatially tagged with the MultiHarp 150 module, that selected the best time-resolution for the different detection time windows. With these settings, PLIM imaging can be performed in two different time regimes: nanoseconds and milliseconds (Figure S14b, Supporting Infor-

The intensity images of CellMask were reconstructed with photons obtained in the 520/35 nm detector arriving in the initial 160 ns in the ns-time regime and during the excitation train of pulses in the ms-time regime. The Ir1 PLIM images were reconstructed with photons in the 550/40 nm detector arriving after 160 ns in the ns-time regime, and by pixelwise fitting the luminescence decay traces to double-exponential functions. The Eu(III) PLIM images were obtained with photons arriving to the 630/60 nm detector 160  $\mu s$  after the excitation pulses in the ms-time regime, and by pixelwise fitting the luminescence decay traces to single-exponential functions. See Figure S14b, Supporting Information for the different time-regimes and representative decay traces.

### **Supporting Information**

Supporting Information is available from the Wiley Online Library or from the author.

## Acknowledgements

This research was financially supported by Projects PID2022-138090NB-C21, TED2021.129598A.I00 and PID2020-114256RB-I00 funded by MICIN/AEI/10.13039/501100011033/ FEDER and by European Union NextGeneration Eu/PRTR the Junta de Andalucía (FQM-195) and FEDER/Junta de Andalucía – Consejería de Transformación Económica, Industria, Conocimiento y Universidades, Project B.CIC.007.UGR23 and the University of Granada (Project PP2022-30B9251101). M. B. and J. R. J. thanks Ministerio de Ciencia Innovación y Universidades for a Ramón y Cajal contracts (grants RYC2019-027692-I and RYC2022-037255-I, respectively) funded by MCIN/AEI/10.13039/501100011033 and FSE+.

#### **Conflict of Interest**

The authors declare no conflict of interest.

#### **Data Availability Statement**

The data that support the findings of this study are available in the supplementary material of this article.

#### **Keywords**

cell imaging,  $d \rightarrow f$  energy transfer,  $Ir^{III}$  complexes, lanthanide nanoparticles

Received: March 4, 2025 Revised: June 3, 2025 Published online: 21951071, 0, Downloaded from https://adarced.onlinelbitary.wiley.com/doi/10.1002/ador.20250717 by Cochametalia, Wiley Online Library on [2906/2025]. See the Terms and Conditions (https://onlinelbitary.wiley.com/terms-and-conditions) on Wiley Online Library for rules of use; OA articles are governed by the applicable Creative Commons Licenses

- [1] M. Wang, Y. Kitagawa, Y. Hasegawa, Chem. Asian J. 2024, 19, 202400038
- [2] Z. Luo, D. Mao, X. Li, J. Luo, C. Gong, X. Liu, Coord. Chem. Rev. 2024, 508 215773
- [3] B. Chen, F. Wang, Trends Chem 2020, 2, 427.
- [4] A. A. Ansari, K. M. Aldajani, A. N. AlHazaa, H. A. Albrithen, Coord. Chem. Rev. 2022, 462, 214523.
- [5] L. Wang, S. Han, C. Li, D. Tu, X. Chen, Acc. Mater. Res. 2023, 4, 193.
- [6] H. H. Gorris, O. S. Wolfbeis, Angew. Chem., Int. Ed. 2013, 52, 3584.
- [7] G. Tessitore, G. A. Mandl, M. G. Brik, W. Park, J. A. Capobianco, Nanoscale 2019, 11, 12015.
- R. Naccache, Q. Yu, J. A. Capobianco, Adv. Opt. Mater. 2015, 3, 482.
- [9] B. L. Abrams, P. H. Holloway, Chem. Rev. 2004, 104, 5783.
- [10] W.-N. Wang, W. Widiyastuti, T. Ogi, I. W. Lenggoro, K. Okuyama, Chem. Mater. 2007, 19, 1723.
- [11] J. C. G. Bünzli, Eur. J. Inorg. Chem. 2017, 2017, 5058.
- [12] S. Wilhelm, ACS Nano 2017, 11, 10644.
- [13] S. Wen, J. Zhou, P. J. Schuck, Y. D. Suh, T. W. Schmidt, D. Jin, Nat. Photon. 2019, 13, 828.
- [14] C. Cheignon, A. A. Kassir, L. K. Soro, L. J. Charbonnière, Nanoscale 2022, 14, 13915.
- [15] C. Falcony, J. U. Balderas, J. Vac. Sci. Technol. B 2019, 37, 028501.
- [16] G. Bao, S. Wen, G. Lin, J. Yuan, J. Lin, K.-L. Wong, J.-C. G. Bünzli, D. Jin, Coord. Chem. Rev. 2021, 429, 213642.
- [17] J. Zhou, J. L. Leaño, Z. Liu, D. Jin, K. Wong, R. Liu, J. G. Bünzli, Small 2018, 14, 1801882.
- [18] Y. Ye, J. Jiménez, M. M. Quesada-Moreno, A. Navarro, E. M. Ortega-Naranjo, A. Orte, J. M. Herrera, Adv. Opt. Mater. 2024, 12, 2302954.
- [19] K. Xu, C. Lin, M.-F. Qin, Z. Yuan, Y. Tao, S.-S. Bao, R. Chen, X. Xie, L.-M. Zheng, ACS Mater. Lett. 2023, 5, 854.
- [20] K. Xu, X. Xie, L.-M. Zheng, Coord. Chem. Rev. 2022, 456, 214367.
- [21] W. Jiang, Y. Gao, Y. Sun, F. Ding, Y. Xu, Z. Bian, F. Li, J. Bian, C. Huang, Inorg. Chem. 2010, 49, 3252.
- [22] B. M. Tissue, Chem. Mater. 1998, 10, 2837.
- [23] E. Garcia-Fernandez, S. Pernagallo, J. A. González-Vera, M. J. Ruedas-Rama, (Ed: J. J. Díaz-Mochón, A. Orte, B. Pedras), Fluorescence in Industry, Springer Ser Fluoresc, Regensburg, 2019, Vol. 18, pp. 213-268.
- [24] A. Ruiz-Arias, F. Fueyo-González, C. Izquierdo-García, A. Navarro, M. Gutiérrez-Rodríguez, R. Herranz, C. Burgio, A. Reinoso, J. M. Cuerva, A. Orte, J. A. González-Vera, Angew. Chem., Int. Ed. 2024, 63, 202314595.

- [25] M. Padial-Jaudenes, M. Tabraue-Chávez, S. Detassis, M. J. Ruedas-Rama, M. C. Gonzalez-Garcia, M. A. Fara, F. J. López-Delgado, J. A. González-Vera, J. J. Guardia-Monteagudo, J. J. Diaz-Mochon, E. Garcia-Fernandez, S. Pernagallo, A. Orte, Sens. Act. B Chem. 2024, 417, 136136.
- [26] J.-T. Mo, Z. Wang, P.-Y. Fu, L.-Y. Zhang, Y.-N. Fan, M. Pan, C.-Y. Su, CCS Chem 2021, 3, 729.
- [27] R. M. Edkins, D. Sykes, A. Beeby, M. D. Ward, Chem. Commun. 2012, 48 9977
- [28] L. K. McKenzie, I. V. Sazanovich, E. Baggaley, M. Bonneau, V. Guerchais, J. A. G. Williams, J. A. Weinstein, H. E. Bryant, Chem.-Eur. *J.* **2017**, *23*, 234.
- [29] H. Huang, S. Banerjee, P. J. Sadler, ChemBioChem 2018, 19, 1574.
- [30] F. Wei, Z. Chen, X.-C. Shen, L. Ji, H. Chao, Chem. Commun. 2023, 59, 6956.
- [31] C. Li, P. Ma, P. Yang, Z. Xu, G. Li, D. Yang, C. Peng, J. Lin, CrystEng-Comm 2011, 13, 1003.
- [32] J. Goetz, A. Nonat, A. Diallo, M. Sy, I. Sera, A. Lecointre, C. Lefevre, C. F. Chan, K.-L. Wong, L. J. Charbonnière, ChemPlusChem 2016, 81, 526.
- [33] D. González Mancebo, A. I. Becerro, A. Corral, M. Moros, M. Balcerzyk, J. M. de la Fuente, M. Ocaña, ACS Omega 2019, 4,
- [34] W. T. Carnall, G. L. Goodman, K. Rajnak, R. S. Rana, J. Chem. Phys. **1989** 90 3443
- [35] K. Binnemans, Coord. Chem. Rev. 2015, 295, 1.
- [36] P. A. Tanner, Chem. Soc. Rev. 2013, 42, 5090.
- [37] A. M. Cross, P. S. May, F. C. J. M. van Veggel, M. T. Berry, J. Phys. Chem. C 2010, 114, 14740.
- [38] X. Zhang, T. Hayakawa, M. Nogami, Int. J. Appl. Ceram. Technol. 2011, 8. 741.
- [39] T. Hayakawa, R. Ikeshita, J. R. Duclère, A. Lecomte, Phys. Status Solidi B 2022, 259, 2100560.
- [40] J. Li, H. Mao, N. Kawazoe, G. Chen, Biomater. Sci. 2017, 5, 173
- [41] Y. Zhang, S. F. Ali, E. Dervishi, Y. Xu, Z. Li, D. Casciano, A. S. Biris, ACS Nano 2010, 4, 3181.
- [42] Y. Li, M. Kröger, W. K. Liu, Nanoscale 2015, 7, 16631.
- [43] N. Dong, Z. Liu, H. He, Y. Lu, J. Qi, W. Wu, J. Controlled Release 2023, 354, 279
- [44] G. Oberdörster, E. Oberdörster, J. Oberdörster, Environ. Health Perspect. 2005, 113, 823.